Chemical Science

ROYAL SOCIETY OF CHEMISTRY

EDGE ARTICLE

View Article Online
View Journal | View Issue

Check for updates

Cite this: *Chem. Sci.*, 2022, **13**, 748

All publication charges for this article have been paid for by the Royal Society of Chemistry

Received 5th December 2021
Accepted 16th December 2021

DOI: 10.1039/d1sc06781h

rsc.li/chemical-science

An organic plastic ferroelectric with high Curie point†

Yong Ai, Peng-Fei Li, Meng-Juan Yang, Yu-Qiu Xu, Meng-Zhen Li and Ren-Gen Xiong *

Plastic ferroelectrics, featuring large entropy changes in phase transitions, hold great potential application for solid-state refrigeration due to the electrocaloric effect. Although conventional ceramic ferroelectrics (*e.g.*, $BaTiO_3$ and $KNbO_3$) have been widely investigated in the fields of electrocaloric material and catalysis, organic plastic ferroelectrics with a high Curie point (T_c) are rarely reported but are of great importance for the sake of environmental protection. Here, we reported an organic plastic ferroelectric, (−)-camphanic acid, which crystallizes in the $P2_1$ space group, chiral polar 2 (C_2) point group, at room temperature. It undergoes plastic paraelectric-to-ferroelectric phase transition with the Aizu notation of 23F2 and high T_c of 414 K, showing large entropy gain ($\Delta S_t = 48.2$ J K^{-1} mol^{-1}). More importantly, the rectangular polarization–electric field (*P–E*) hysteresis loop was recorded on the thin film samples with a large saturated polarization (P_s) of 5.2 μC cm^{-2}. The plastic phase transition is responsible for its multiaxial ferroelectric feature. This work highlights the discovery of organic multiaxial ferroelectrics driven by the motive of combining chirality and plastic phase transition, which will extensively promote the practical application of such unique functional materials.

Introduction

The research and practical application of ferroelectrics have been dominated by ceramic perovskite oxides[1,2] for a long time since the first ferroelectric Rochelle salt was discovered in 1921.[3] However, many of these ferroelectrics are discovered as uniaxial, which is a major obstacle to improving their thin film performance.[4] By contrast, organic molecules with ease of preparation and mechanical flexibility bring great prospects.[5–8] Among them, plastic crystals seem to be quite suitable for discovery of the multiaxial ferroelectrics because spherical organic molecular structures with highly symmetric high-temperature phases are prone to trigger solid–solid phase transitions accompanying dramatic symmetry breaking.[9,10] That is to say, when plastic crystals possess ferroelectricity, they usually exhibit multiaxial ferroelectric properties.[9,11]

Plastic ferroelectrics, characterized by their unique polarization *versus* electric field (*P–E*) hysteresis and the plastic phase transition, have a widespread growing interest in the fields of materials science and energy science.[9,11,12] The typical inherent aspect of the plastic ferroelectric is the large entropy change during the paraelectric to ferroelectric phase transition.[13–15] For instance, the plastic ferroelectric ionic crystals tetramethylammonium tetrachloroferrate(III) and tetramethylammonium bromotrichloroferrate(III) show giant entropy change values (ΔS) at the phase II/I transition, which are consistent with this notion.[16] Such extremely large entropy changes associated with the molecular order–disorder phase transition that occurs in electrocaloric materials have been extensively investigated for cooling purposes.[17–19] Therefore, plastic ferroelectric crystals could be a potential alternative to conventional refrigeration materials (Freon), which damage the ozone layer.

Research on organic plastic ferroelectrics has emerged in very recent years.[20–22] In 2016, Harada *et al.* reported the first plastic ferroelectric crystal, quinuclidinium perrhenate.[23] Thanks to the tunability of the crystal orientation and the ability of mechanical deformation, the excellent ferroelectric characteristics of quinuclidinium perrhenate were exhibited in the film and sheet forms. Then a series of perrhenate-based plastic/ferroelectrics were reported.[24,25] The globular organic molecules composed of tetramethylammonium or quinuclidinium cations have extensively been employed to construct the plastic ferroelectrics, such as tetraethylammonium perchlorate,[11] [3.2.1-dabco]BF_4,[26] [Hdabco]ClO_4,[27] [Hdabco]BF_4,[28] ammonia borane derivatives,[21,29] *etc.* In addition to the above-mentioned molecular ionic crystals, single-component organic 2-(hydroxymethyl)-2-nitro-1,3-propanediol with low molecular mass exhibits plastic ferroelectricity and 48 crystallographically equivalent polarization directions, which is the most among all ferroelectrics.[30,31] The chemical design of organic ferroelectrics with a chiral center endowed the crystal

---

Ordered Matter Science Research Center, Nanchang University, Nanchang 330031, P. R. China. E-mail: xiongrg@seu.edu.cn

† Electronic supplementary information (ESI) available. CCDC 2108436 and 2108441. For ESI and crystallographic data in CIF or other electronic format see DOI: 10.1039/d1sc06781h

with a particular inherent chirality,[32–36] which seems to be impossible to achieve from the ceramic ferroelectrics. Although great achievements have been made on these molecular ionic plastic ferroelectrics, chiral small organic molecules have rarely been discovered as plastic ferroelectrics.

Here, in this work, we discovered an organic multiaxial plastic ferroelectric, (−)-camphanic acid, with a phase transition temperature as high as 414 K (above that of $BaTiO_3$ $T_c = 393$ K).[37] (−)-Camphanic acid crystalizes in the $P2_1$ space group, chiral polar point group 2 (C_2), at room temperature. It exhibits a $23F2$ type ferroelectric phase transition, showing a sharp step-like dielectric anomaly, low coercive field (50 kV cm^{-1}) and identical ferroelectric domains. More importantly, its rectangular polarization–electric field (*P*–*E*) hysteresis loops were recorded on thin-film samples with a respective large saturated polarization of 5.2 μC cm^2, confirming the ferroelectricity in the polycrystalline states. The plastic phase transition large entropy gain ($\Delta S_t = 48.2$ J K^{-1} mol^{-1}) is responsible for its multiaxial ferroelectric feature. This finding reveals the enormous benefits of plastic ferroelectrics and sheds light on exploring single component organic ferroelectrics.

Results and discussion

The colourless needle shape crystals were obtained by slowly evaporating the methanol solution of (−)-camphanic acid at room temperature in one week (Fig. S1†). Differential scanning calorimetry (DSC) is an efficient way to measure the reversible structural phase transition behaviour by detecting the exothermal and endothermal transformations. As shown in Fig. 1a, the DSC anomalies of (−)-camphanic acid were observed during the heating-cooling cycles. The peak temperature of the endothermic peak in the heating run indicates that the phase transition point (T_c) was 414 K, which is higher than that of the typical ceramic ferroelectric $BaTiO_3$ ($T_c = 393$ K).[37] Notably, the temperature-dependent hysteresis or tailing effect in the cooling runs is typical of the phase transition behaviour. For convenience, the phase above 414 K was labelled as the high-temperature phase (HTP) and the phase below as the low-temperature phase (LTP). The thermogravimetric analysis (TGA) measurement of (−)-camphanic acid shows that decomposing occurred at around 510 K (Fig. S2†), indicating its superior thermal stability.

Note that there is a clear shoulder peak in the DSC heating trace at around 406 K. In order to make sure the origin of this unexpected shoulder peak, we conducted the powder X-ray diffraction (PXRD) measurements. The shaded area in Fig. S3b† shows the peaks at 14, 15, and 16.3 degrees. It is worthy of note that 14 and 16.3 degrees could be taken as the characteristic peaks of the LTP, while 15 degree for the HTP. Apparently, (−)-camphanic acid undergoes the phase transition between 406 K and 420 K with the fact that peaks at 14, 15, and 16.3 degrees are observed at these temperatures. Therefore, the shoulder peak is mainly due to the pre-transitional contribution, which is commonly observed in the literature studies.[38–40] Then the main peak splits into two parts through Gaussian fitting (Fig. S4†). The integration area of the shoulder peak has only 5% of the whole endothermic peak. However the main peak at 414 K due to the plastic phase transition possesses 95% of the endothermic peak area.

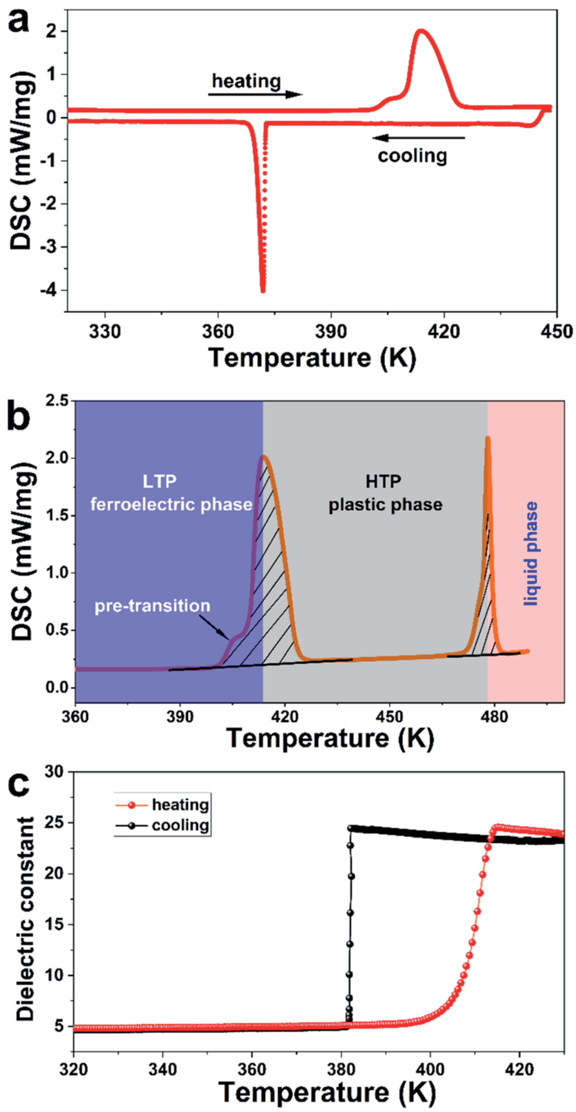

Fig. 1 Phase transition behaviors of (−)-camphanic acid. (a) DSC curves in the heating-cooling runs. (b) Single heating run DSC curve, scan rate, 5 K min^{-1}. Color shaded areas refer to the LTP, HTP and liquid phases. The entropy changes of plastic transitions in the crystal lattice beyond that of melting. Shaded area: the heat capacity anomaly assumed as the vacancy formation. (c) Temperature-dependent dielectric constant (real part ε') measured at 1 MHz.

To get a deep insight into the phase transitions, we analysed the DSC curve in a single heating run to investigate the endothermal features. The integration area of the fit peak 2 is taken as the entropy changes for the plastic phase transition (Fig. S4†). In Fig. 1b, the entropy changes for its plastic solid to solid and melting phase transitions are 48.2 and 12.9 J mol^{-1} K^{-1}, respectively. The entropy changes of the structural phase transition (ΔS_t) are almost 3.7 times higher than that of melting (ΔS_m), confirming the plastic phase transition feature. Such a large ΔS_t value and $\Delta S_t/\Delta S_m$ ratio are commonly observed in the plastic phase transition.[14,15] The phase transition was usually accompanied with a large gain in orientation possibilities described by the Boltzmann relation $\Delta S = R\ln(n_H/n_L)$, where R is the gas constant, n_H and n_L represent the numbers of orientations in the low- and high-temperature phases, respectively.[41,42] The ratio n_H/n_L was calculated to be as high as 326 for (−)-camphanic acid. Such values are much higher than those for plastic crystals of cubane ($n_H/n_L = 6$),[43] adamantine ($n_H/n_L = 7$),[44] neopentane ($n_H/n_L = 9$),[45] cyclohexanol ($n_H/n_L = 55$),[46] (*R*)-3-quinuclidinol ($n_H/n_L = 65$),[35] and C_{60} ($n_H/n_L = 240$).[41]

The plastic transition behaviour was then determined by the plot of the temperature-dependent dielectric anomaly. The real part of the dielectric constant *versus* temperature measured at 1 MHz is shown in Fig. 1c. The step fashion dielectric anomalies indicate that the dominant phase transition occurs at 414 K for (−)-camphanic acid, which is in good agreement with the above-mentioned T_c deduced from DSC measurement. Moreover, the cooling curve of the temperature-dependent dielectric constant (real part ε') is sharper than the heating one, see Fig. 1c. It is worthy of note that the shape of the endothermic peak (heating) is wider than that of the exothermic peak (cooling), as shown in Fig. 1a. Apparently, the temperature window for the phase transition from the plastic to the ferroelectric phase (cooling process) is much narrower than that for the transition from the ferroelectric to the plastic phase (heating process). The plausible reason for such sharper curve ε' during the cooling process could be there exists the pre-transitional stage before 406 K during heating, see the DSC analysis.

The paraelectric to ferroelectric phase transition accompanying the crystal structural symmetry breaking usually lead to the formation of strong dipole moments and polarization of the crystal.[10] To better understand the plastic phase transition, single-crystal X-ray diffraction measurements were carried out at various temperatures. (−)-Camphanic acid crystallized in the monoclinic crystal system in the LTP (100 K and 373 K), see Table S1, ESI.† At 100 K, the crystal structure was refined in the polar space group $P2_1$, 2-point group, with cell parameters of $a = 6.29835(9)$ Å, $b = 10.64131(14)$ Å, $c = 7.53892(11)$ Å, $\beta = 103.5036(14)°$, $Z = 2$, and $V = 491.311(12)$ Å^3. As shown in Fig. 2a, the asymmetric unit of (−)-camphanic acid in the LTP contains one single molecule. The C atoms marked with asterisk '*' have the '*S*' chirality and contribute the whole '*S*' conformation of the molecular packing of (−)-camphanic acid. Fig. 2b shows the packing view of (−)-camphanic acid in the one-unit cell. There exists intermolecular hydrogen bonding O–H⋯O formed by the carboxylic group as the donor and carbonyl group as the accepter. It is worth mentioning that hydrogen bonding is beneficial to the stabilization of ordered molecules in the LTP and thus greatly contributes to the high T_c of the crystal[47,48] and further reservation of its ferroelectricity at a higher temperature.[49]

We then performed the single-crystal measurement at 420 K (above T_c) to probe the structure in the HTP. Due to the highly disordered feature of the plastic phase, it is difficult to determine the single-crystal structure at high-temperature. Besides, the mild sublimation of the crystals also caused the failure in the crystal data collection. To further determine the structure of (−)-camphanic acid, we performed the PXRD measurements. The experimental PXRD pattern matched well with the one simulated from the single crystal structure at room temperature (Fig. S5†), suggesting the high crystallinity and purity of the corresponding phase. Then, PXRD was performed in the HTP to assist the structural analysis (Fig. S3a†). The number of peaks in the HTP decreased compared to that in the LTP. The disappearance of the PXRD peaks in the HTP indicates a highly symmetric phase. Pawley refinements of the PXRD of (−)-camphanic acid suggest a plausible cubic lattice system for the HTP.

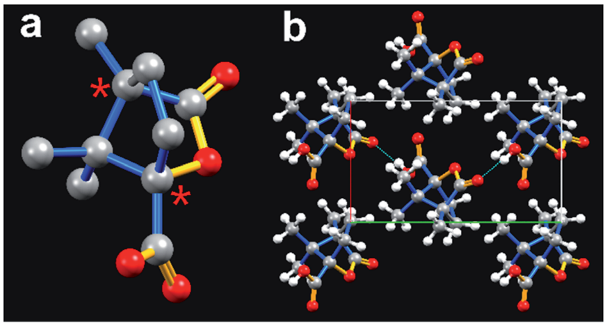

Fig. 2 (a) Asymmetric unit of the molecular structure of (−)-camphanic acid. H atoms were omitted for clarity. (b) Packing view of (−)-camphanic acid in the one-unit 7 viewing from the 'ab' plane. The red dot lines represent the hydrogen bonding O–H⋯O. Red: O atom, white: H atom, and dark gray: C atom.

It is worth mentioning that solid materials crystallizing in the noncentrosymmetric point groups (except for 432, 422 and 622) are second harmonic generation (SHG) active, according to Kleinman symmetry rules.[50] The SHG measurements are widely carried out to detect the polar properties of the single crystal. (−)-Camphanic acid possesses 25% SHG intensity of that of the potassium dihydrogen phosphate (KDP) at room temperature (Fig. S6†). To further confirm the phase transition behaviour associated with the symmetry breaking, the temperature-dependent SHG signal was monitored. As depicted in Fig. S7†, (−)-camphanic acid was SHG active in a wide temperature range before melting. Therefore, (−)-camphanic acid should crystallize in the 23-point group in the HTP. The significant variation of the PXRD patterns from the LTP to the HTP with the symmetry change of 23*F*2 strongly reveals the ferroelectric phase transition of (−)-camphanic acid.

To examine the ferroelectricity of (−)-camphanic acid, we obtained the polarization–electric (*P*–*E*) hysteresis loop by using the so-called double wave method[51,52] at room temperature. As shown in Fig. 3a, a typical rectangular-shaped *P*–*E* hysteresis loop was obtained, which directly demonstrates its ferroelectricity. The measured remnant polarization (P_r) and saturated polarization (P_s) are around 5.2 μC cm^{-2}, comparable to that of molecular ferroelectrics with a plastic phase transition, such as tetramethylammonium tetrachloroferrate(III) (7.2 μC cm^{-2}),[11] tetraethylammonium perchlorate (4.5 μC cm^{-2}),[16] quinuclidinium perrhenate (3.5 μC cm^{-2}),[23] and so on. According to Aizu rules,[53] there are 6 equivalent ferroelectric polarization directions for the 23*F*2 type paraelectric to ferroelectric phase transition, as shown in Fig. 3b.

Then, we performed the piezoresponse force microscopy (PFM)[54] study of domain imaging and polarization switching on

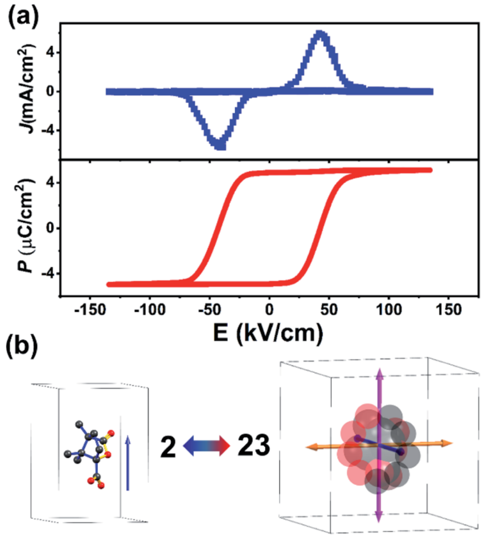

Fig. 3 (a) Ferroelectric hysteresis loops of (−)-camphanic acid measured on the thin film sample using the double wave method at room temperature. (b) The scheme drawing of the possible equivalent polarization directions in the ferroelectric phase (2-point group) and paraelectric phase (23-point group), respectively.

the (−)-camphanic acid thin film. For annealing, the thin film sample was heated to the paraelectric phase and then cooled to room temperature. Fig. 4 shows the lateral and vertical PFM images. The ferroelectric domains were randomly distributed with no domain pattern correlated with the surface morphology. The lateral PFM images show that the domains are distinguished by the colour tones in the phase image (Fig. 4a) and the clear domain walls in the amplitude image (Fig. 4b), which suggests that there exist various in-plane polarization orientations. The domain pattern of the vertical PFM images (Fig. 4d and e) is completely different from the lateral one, which can be attributed to the multiaxial polar nature of (−)-camphanic acid.

To further investigate the ferroelectric properties by PFM, we carried out domain switching measurements in the (−)-camphanic acid thin film. Fig. 5a shows the multi-domain structure. The switching of the in-plane component of the polarization is depicted in Fig. 5b, where a tip voltage of +150 V is applied on the blue box region. The predominant contrast in the written region reveals the in-plane polarization flipping. Then, the same region was poled with a reverse tip voltage of −150 V (Fig. 5c). As expected, some part of the in-plane domain is again flipped to that shown in Fig. 5b. Therefore, the reversal of phase-contrast confirms the switching of polarization. The detailed PFM information including the topography and amplitude images is shown in Fig. S8.† In addition, no change was observed in the surface morphology after the electric poling and the amplitude images match well with the corresponding phase images. Fig. 5d and e show the local PFM switching hysteresis recorded on the thin film. The well-defined butterfly loops of the PFM amplitude signals and the distinct 180° switching of the phase signals are the typical signature of ferroelectric switching of (−)-camphanic acid.

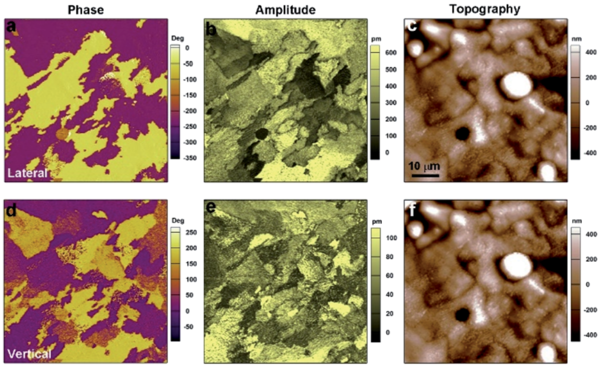

Fig. 4 Domain structure observed in the (−)-camphanic acid thin film. (a and d) Phase, (b and e) amplitude, and (c and f) topographic images were obtained in (a–c) lateral and (d–f) vertical PFM modes.

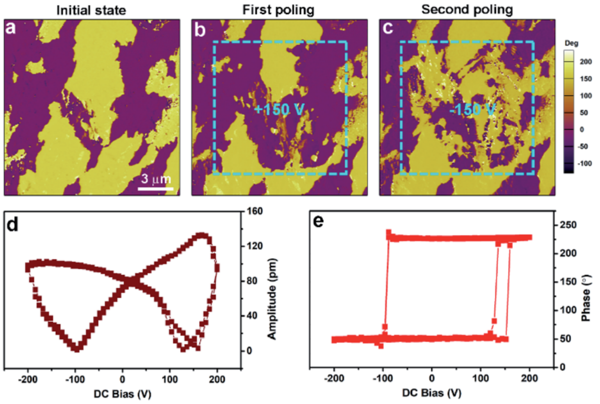

Fig. 5 Polarization switching measurements for the (−)-camphanic acid thin film. (a–c) Lateral PFM phase images of the initial state (a), after poling the blue box region with a tip voltage of +150 V (b) and after poling the same region with a tip voltage of −150 V (c). (d and e) PFM switching spectroscopy loops.

Conclusions

In summary, we have reported an organic plastic ferroelectric (−)-camphanic acid. Briefly, (−)-camphanic acid exhibits a high Curie temperature (414 K), large saturated polarization of 5.2 μC cm^{-2} and low coercive field (50 kV cm^{-1}). The plastic phase transition with a large entropy gain, $\Delta S_t = 48.2$ J K^{-1} mol^{-1} (much higher than its fusion entropy, 12.9 J mol^{-1} K^{-1}) is responsible for its multiaxial polarization feature. This work highlights the discovery of organic molecular ferroelectrics with the concept of introducing chirality and plastic phase transition. The combination of numerous globular polar molecules and chirality will undoubtedly broaden the organic plastic ferroelectric family and opens an avenue for exploring their application for solid-state refrigeration.

Data availability

The experimental data supporting this article have been uploaded as part of the ESI.†

Author contributions

Ren-Gen Xiong devised and developed the project. Yong Ai, Peng-Fei Li, Meng-Juan Yang, Yu-Qiu Xu and Meng-Zhen Li performed the experiments. All the authors analysed the data, discussed the results and contributed to the manuscript.

Conflicts of interest

There are no conflicts to declare.

Acknowledgements

This work was supported by the National Natural Science Foundation of China (21901099 and 21991141).

Notes and references

1 C. Qiu, B. Wang, N. Zhang, S. Zhang, J. Liu, D. Walker, Y. Wang, H. Tian, T. R. Shrout, Z. Xu, L.-Q. Chen and F. Li, *Nature*, 2020, **577**, 350–354.

2 G. H. Haertling, *J. Am. Chem. Soc.*, 1999, **82**, 797–818.

3 J. Valasek, *Phys. Rev.*, 1921, **17**, 475.

4 W. Zhang and R.-G. Xiong, *Chem. Rev.*, 2012, **112**, 1163–1195.

5 D. W. Fu, H. L. Cai, Y. Liu, Q. Ye, W. Zhang, Y. Zhang, X. Y. Chen, G. Giovannetti, M. Capone, J. Li and R. G. Xiong, *Science*, 2013, **339**, 425–428.

6 W. Q. Liao, Y. Y. Tang, P. F. Li, Y. M. You and R. G. Xiong, *J. Am. Chem. Soc.*, 2017, **139**, 18071–18077.

7 Y. Zhang, Y. Liu, H. Y. Ye, D. W. Fu, W. Gao, H. Ma, Z. Liu, Y. Liu, W. Zhang, J. Li, G. L. Yuan and R. G. Xiong, *Angew. Chem., Int. Ed. Engl.*, 2014, **53**, 5064–5068.

8 Z. X. Zhang, H. Y. Zhang, W. Zhang, X. G. Chen, H. Wang and R. G. Xiong, *J. Am. Chem. Soc.*, 2020, **142**, 17787–17794.

9 J. Harada, *APL Mater.*, 2021, **9**, 020901.

10 P.-P. Shi, Y.-Y. Tang, P.-F. Li, W.-Q. Liao, Z.-X. Wang, Q. Ye and R.-G. Xiong, *Chem. Soc. Rev.*, 2016, **45**, 3811–3827.

11 H.-Y. Ye, J.-Z. Ge, Y.-Y. Tang, P.-F. Li, Y. Zhang, Y.-M. You and R.-G. Xiong, *J. Am. Chem. Soc.*, 2016, **138**, 13175–13178.

12 R. A. Surmenev, R. V. Chernozem, I. O. Pariy and M. A. Surmeneva, *Nano Energy*, 2021, **79**, 105442–105465.

13 Y. Kaneko and M. Sorai, *Phase Transitions*, 2007, **80**, 517–528.

14 J. Timmermans, *J. Phys. Chem. Solids*, 1961, **18**, 1–8.

15 D. Chandra, W. Ding, R. A. Lynch and J. J. Tomilinson, *J. Less-Common Met.*, 1991, **168**, 159–167.

16 J. Harada, N. Yoneyama, S. Yokokura, Y. Takahashi, A. Miura, N. Kitamura and T. Inabe, *J. Am. Chem. Soc.*, 2018, **140**, 346–354.

17 E. Defay, R. Faye, G. Despesse, H. Strozyk, D. Sette, S. Crossley, X. Moya and N. D. Mathur, *Nat. Commun.*, 2018, **9**, 1827–1835.

18 G. Zhang, Q. Li, H. Gu, S. Jiang, K. Han, M. R. Gadinski, M. A. Haque, Q. Zhang and Q. Wang, *Adv. Mater.*, 2015, **27**, 1450.

19 J. J. Wang, D. Fortino, B. Wang, X. Zhao and L. Q. Chen, *Adv. Mater.*, 2020, **32**, 1906224.

20 Y.-Y. Tang, P.-F. Li, W.-Q. Liao, P.-P. Shi, Y.-M. You and R.-G. Xiong, *J. Am. Chem. Soc.*, 2018, **140**, 8051–8059.

21 H.-Y. Liu, H.-Y. Zhang, X.-G. Chen and R.-G. Xiong, *J. Am. Chem. Soc.*, 2020, **142**, 15205–15218.

22 H.-Y. Zhang, Y.-Y. Tang, P.-P. Shi and R.-G. Xiong, *Acc. Chem. Res.*, 2019, **52**, 1928–1938.

23 J. Harada, T. Shimojo, H. Oyamaguchi, H. Hasegawa, Y. Takahashi, K. Satomi, Y. Suzuki, J. Kawamata and T. Inabe, *Nat. Chem.*, 2016, **8**, 946–952.

24 J. Harada, Y. Kawamura, Y. Takahashi, Y. Uemura, T. Hasegawa, H. Taniguchi and K. Maruyama, *J. Am. Chem. Soc.*, 2019, **141**, 9349–9357.

25 Y.-Y. Tang, P.-F. Li, P.-P. Shi, W.-Y. Zhang, Z.-X. Wang, Y.-M. You, H.-Y. Ye, T. Nakamura and R.-G. Xiong, *Phys. Rev. Lett.*, 2017, **119**, 207602.

26 Z.-H. Wei, Z.-T. Jiang, X.-X. Zhang, M.-L. Li, Y.-Y. Tang, X.-G. Chen, H. Cai and R.-G. Xiang, *J. Am. Chem. Soc.*, 2020, **142**, 1995–2000.

27 Y.-Y. Tang, W.-Y. Zhang, P.-F. Li, H.-Y. Ye, Y. M. You and R.-G. Xiong, *J. Am. Chem. Soc.*, 2016, **138**, 15784–15789.

28 P.-P. Shi, Y.-Y. Tang, P.-F. Li, H.-Y. Ye and R.-G. Xiong, *J. Am. Chem. Soc.*, 2017, **139**, 1319–1324.

29 A. Mondal, B. Bhattacharya, S. Das, S. Bhunia, R. Chowdhury, S. Dey and C. M. Reddy, *Angew. Chem., Int. Ed.*, 2020, **132**, 11064–11073.

30 Z. Sun, T. Chen, X. Liu, M. Hong and J. Luo, *J. Am. Chem. Soc.*, 2015, **137**, 15660–15663.

31 Y. Ai, Y.-L. Zeng, W.-H. He, X.-Q. Huang and Y.-Y. Tang, *J. Am. Chem. Soc.*, 2020, **142**, 13989–13995.

32 Y. Ai, X.-G. Chen, P.-P. Shi, Y.-Y. Tang, P.-F. Li, W.-Q. Liao and R.-G. Xiong, *J. Am. Chem. Soc.*, 2019, **141**, 4474–4479.

33 B.-B. Deng, C.-C. Xu, T.-T. Cheng, Y.-T. Yang, Y.-T. Hu, P. Wang, W.-H. He, M.-J. Yang and W.-Q. Liao, *J. Am. Chem. Soc.*, 2020, **142**, 6946–6950.

34 D.-W. Fu, J.-X. Gao, W.-H. He, X.-Q. Huang, Y.-H. Liu and Y. Ai, *Angew. Chem., Int. Ed.*, 2020, **59**, 17477–17481.

35 P.-F. Li, W.-Q. Liao, Y.-Y. Tang, W. Qiao, D. Zhao, Y. Ai, Y.-F. Yao and R.-G. Xiong, *Proc. Natl. Acad. Sci. U. S. A.*, 2019, **116**, 5878–5885.

36 P.-F. Li, Y. Ai, Y.-L. Zeng, J.-C. Liu, Z.-K. Xu and Z.-X. Wang, *Chem. Sci.*, 2021, DOI: 10.1039/d1sc04322f.

37 K.-i. Sakayori, Y. Matsui, H. Abe, E. Nakamura, M. Kenmoku, T. Hara, D. Ishikawa, A. Kokubu, K.-i. Hirota and T. Ikeda, *Jpn. J. Appl. Phys.*, 1995, **34**, 5443–5445.

38 M. Szafrański, *Cryst. Growth Des.*, 2016, **16**, 3771–3776.

39 P. Szklarz, A. Ingram, Z. Czapla, C. Górecki and M. Szafrański, *Phase Transitions*, 2017, **90**, 610–617.

40 M. Szafrański, *J. Phys. Chem. B*, 2011, **115**, 8755–8762.

41 Y. Miyazaki, M. Sorai, R. Lin, A. Dworkin, H. Szwarc and J. Godard, *Chem. Phys. Lett.*, 1999, **305**, 293–297.

42 Q. Pan, Z.-B. Liu, Y.-Y. Tang, P.-F. Li, R.-W. Ma, R.-Y. Wei, Y. Zhang, Y.-M. You, H.-Y. Ye and R.-G. Xiong, *J. Am. Chem. Soc.*, 2017, **139**, 3954–3957.

43 M. A. White, R. E. Wasylishen, P. E. Eaton, Y. Xiong, K. Pramod and N. Nodari, *J. Phys. Chem.*, 1992, **96**, 421–425.

44 S.-S. Chang and E. F. Westrum Jr, *J. Phys. Chem.*, 1960, **64**, 1547–1551.

45 J. G. Aston and G. H. Messerly, *J. Am. Chem. Soc.*, 1936, **58**, 2354–2361.
46 K. Adachi, H. Suga and S. Seki, *Bull. Chem. Soc. Jpn.*, 1968, **41**, 1073–1087.
47 K. Matuszek, R. Vijayaraghavan, M. Kar and D. R. MacFarlane, *Cryst. Growth Des.*, 2020, **20**, 1285–1291.
48 R. D. McGillicuddy, S. Thapa, M. B. Wenny, M. I. Gonzalez and J. A. Mason, *J. Am. Chem. Soc.*, 2020, **142**, 19170–19180.
49 S. Horiuchi, Y. Tokunaga, G. Giovannetti, S. Picozzi, H. Itoh, R. Shimano, R. Kumai and Y. Tokura, *Nature*, 2010, **463**, 789–792.
50 D. Kleinman, *Phys. Rev.*, 1962, **126**, 1977.
51 M. Fukunaga and Y. Noda, *J. Phys. Soc. Jpn.*, 2008, **77**, 064706.
52 M. Fukunaga and Y. Noda, *J. Korean Phys. Soc.*, 2009, **55**, 888–892.
53 K. Aizu, *J. Phys. Soc. Jpn.*, 1969, **27**, 387–396.
54 H.-Y. Zhang, X.-G. Chen, Y.-Y. Tang, W.-Q. Liao, F.-F. Di, X. Mu, H. Peng and R.-G. Xiong, *Chem. Soc. Rev.*, 2021, **50**, 8248–8278.